Transport Properties of a Two-Dimensional PbSe Square Superstructure in an Electrolyte-Gated Transistor

Alimoradi Jazi, M.; Janssen, V. A.E.C.; Evers, W. H.; Tadjine, A.; Delerue, C; Siebbeles, L. D.A.; Van Der Zant, H. S.J.; Houtepen, A. J.; Vanmaekelbergh, D

Important note
To cite this publication, please use the final published version (if applicable).
Please check the document version above.

NANO LETTERS

Transport Properties of a Two-Dimensional PbSe Square Superstructure in an Electrolyte-Gated Transistor

M. Alimoradi Jazi,[⊥,†] V. A. E. C. Janssen,[⊥,‡] W. H. Evers,[‡] A. Tadjine,[∥] C. Delerue,[∥] L. D. A. Siebbeles,[§] H. S. J. van der Zant,[‡] A. J. Houtepen,[§] and D. Vanmaekelbergh[*,†]

[†]Debye Institute for Nanomaterials Science, University of Utrecht, Princetonplein 1, 3584 CC Utrecht, The Netherlands
[‡]Kavli Institute of Nanoscience, Delft University of Technology, 2628 CJ Delft, The Netherlands
[§]Optoelectronic Materials Section, Department of Chemical Engineering, Delft University of Technology, Van der Maasweg 9, 2629 HZ Delft, The Netherlands
[∥]IEMN-Department of ISEN, UMR CNRS 8520, 59046 Lille, France

S *Supporting Information*

ABSTRACT: Self-assembled nanocrystal solids show promise as a versatile platform for novel optoelectronic materials. Superlattices composed of a single layer of lead–chalcogenide and cadmium–chalcogenide nanocrystals with epitaxial connections between the nanocrystals, present outstanding questions to the community regarding their predicted band structure and electronic transport properties. However, the as-prepared materials are intrinsic semiconductors; to occupy the bands in a controlled way, chemical doping or external gating is required. Here, we show that square superlattices of PbSe nanocrystals can be incorporated as a nanocrystal monolayer in a transistor setup with an electrolyte gate. The electron (and hole) density can be controlled by the gate potential, up to 8 electrons per nanocrystal site. The electron mobility at room temperature is 18 cm^2/(V s). Our work forms a first step in the investigation of the band structure and electronic transport properties of two-dimensional nanocrystal superlattices with controlled geometry, chemical composition, and carrier density.

KEYWORDS: *2D superstructure, self-assembly, oriented attachment, electrolyte gating, optoelectrical characterization*
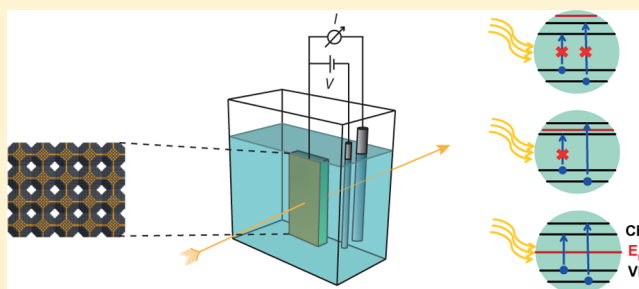
The optoelectronic properties of nanocrystal (NC) solids have been extensively investigated in the past decade. These systems are generally prepared by the assembly of NCs from a nearly monodisperse suspension. Once assembled in the solid phase, the individual NC building blocks are separated by (in)organic capping molecules, forming a tunnel barrier for the charge carriers.[1−11] The nature and length of the capping determines the width and height of the tunneling barriers and hence the dot-to-dot tunneling rates and carrier mobility.[12−15] By advanced engineering, reasonable carrier mobilities (0.1−20 cm^2/(V s)) have been reached in NC solids.[4,16−24] These three-dimensional (3D) films consist of NC quantum dots that are coupled via ligands in three dimensions. They are important for understanding (hopping-controlled) electron transport and for applications in 3D optoelectronic devices such as solar cells and LEDS. Here, we present an optoelectronic study of a genuine 2D superlattice, a PbSe NC monolayer sheet of (truncated) cubic nanocrystals that are epitaxially connected and thus electronically coupled in the lateral directions only via their {100} facets. Quantum confinement prevails in the direction perpendicular to the sheet. It is important to realize that the effect of the lateral nanogeometry on the band structure is very strong in such systems. We remark that a study of a similar

superlattice, however consisting of several NC monolayers has been presented in ref 29. The evolution of the band structure in a bi- and multilayer superlattice is presented in the SI (Figure S4).

Recently, two-dimensional Pb-chalcogenide (PbS, PbSe, PbTe) systems have been prepared by interfacial nanocrystal assembly and attachment.[25,26] These systems consist of nanocrystals that are epitaxially connected via specific facets; this results in quantum wells[27] or 2D systems with a square or honeycomb arrangement of the nanocrystals.[25] In square 2D lattices, the nanocrystals are epitaxially connected via the {100} facets. This oriented attachment process results in a square superstructure in which the voids are due to the truncated cubic shape of the NC building blocks. The electronic coupling in these systems is determined by the size of the PbSe crystalline neck, and a substantially larger electronic coupling is expected compared to NC solids in which the crystals are connected by ligands.[28,29] Calculations show that provided that the coupling between the crystals is strong enough a novel material is
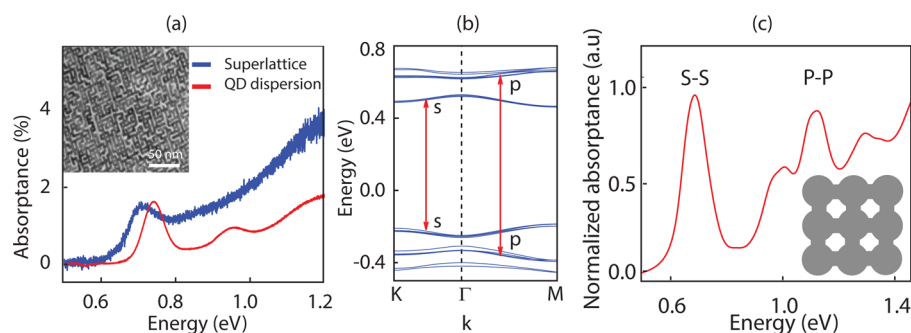
Figure 1. (a) Absorption spectrum of a monolayer of a square PbSe superlattice annealed at 80 °C. The red curve shows the absorption of a suspension of nanocrystals as a reference. Inset: Transmission electron microscope image of a part of a PbSe square lattice (monolayer) prepared by self-assembly and oriented attachment at 80 °C; the scale bar indicates 50 nm. (b) Tight-binding band structure for a square superlattice. The S–S and P–P valence-to-conduction band optical transitions are indicated with arrows and these lead to the first two absorption features in panel c. (c) Calculated tight-binding absorption spectrum for a square PbSe superlattice. Inset: geometry used for the calculation. The nanocrystals are modeled as spheres with a diameter of 5.5 nm. The spheres are connected by cylinders of 2.2 nm in length.

developed with a geometry-specific band-structure.[28] In that respect, it has recently been calculated that two-dimensional superstructures with a honeycomb geometry show Dirac-type valence- and conduction bands, combining semiconductor properties with those of graphene.[30] However, from an electronic viewpoint the as-prepared 2D superlattices are intrinsic semiconductors. To populate the conduction (valence) bands with electrons (holes) in a controlled way, chemical doping or external gating is required. Here, we show that square superlattices of PbSe nanocrystals, which were self-assembled on top of a liquid substrate, can be transferred and incorporated as a nanocrystal monolayer in a transistor setup with an electrolyte gate.

We studied the injection of carriers by using three types of liquid electrolyte gating. We found that provided the PbSe surface is protected from oxygen and water electrons can be reversibly injected and extracted up to about eight electrons/NC site. Thus, the lowest conduction bands of the superstructure become occupied. In two-probe measurements, we find a rapid rise of the electron mobility up to 5 cm²/(V s). A four-probe geometry eliminates the contact resistance and enables measurements on small, more homogeneous sheets. In a monolayer of the superstructure, we then measure an electron mobility as high as 18 cm²/(V s).

Formation of a 2D Square Superlattice. PbSe superlattices are formed by assembling PbSe nanocrystals in a monolayer at the toluene suspension air/interface after which the nanocrystals attach via their four vertical {100} facets. The mechanism has been reported recently[31] (details in SI). After the oriented attachment, the superlattice was annealed at 80 °C for 20 min for the differential capacitance measurements and annealed stepwise at 30°, 50°, and 80° for each 15 min for the optical bleach and four-probe measurements. A part of a monolayer sheet is shown in the inset of Figure 1a. The absorption spectrum of such a single layer is presented in Figure 1a. It can be seen that the absorption peak shows a red shift and a broadening compared to PbSe NCs in suspension. The red shift is due to polarization effects.[32] The peak broadening is caused by the quantum mechanical coupling between the NCs in the superlattice.[18] The absorptivity of the monolayer is about 1.5%; this is in good agreement with optical transitions in a quantum membrane as reported recently.[33]

Figure 1b shows the band structure obtained from a tight-binding (TB) calculation. The calculated absorption spectrum, depicted in Figure 1c, shows a first peak related to the transitions between the S-type envelope functions and a second peak corresponding to the transitions between the P-type envelope functions. The experimental absorption spectrum shows a similar peak at 0.7 eV. This peak can now be related to the valence-to-conduction band transitions involving the band resulting from coupling of the S-type envelope functions. It is important to note that the S-bands in Figure 1b are 8-fold degenerate.

The 2D PbSe NC monolayer superstructure (see Figure 1a, inset) is scooped from the ethylene glycol substrate and is put on top of the transistor electrodes by horizontal contact approaching with the device from above. The quality and uniformity of the superlattice sheet is checked by visual inspection. To enable a relation between the electrical transport properties and the atomic structure of the superlattice, a part of the NC superstructure was put on a TEM grid for structural characterization (see Figure S2).

Optical and Electrical Characterization of the Super-lattice in a Transistor. To investigate the behavior of the quantum-dot superlattice with a liquid gate, three independent experiments were performed. By means of an optical bleaching experiment and a differential capacitance measurement the carrier density has been quantified. The sheet conductance was determined by two- and four-probe conductance measurements in a Hall-bar geometry. These three different experiments require different chip designs; Figure S3 shows their schematic representations. All three designs are gold structures patterned on a Si–SiO₂ wafer by optical or e-beam lithography. The three different experiments use a different electrolyte and a different gating setup.

In all devices, the material is contacted by a source and drain electrode; the area in between the source and drain is the active channel of the device. An applied potential difference between the channel and the gate causes ions of opposing polarities to migrate to the surface of the gate and to the surface of the sample. Near the sample, the ions form an electrical double layer. This electrical double layer can induce carrier densities that outperform a conventional back gate by an order of magnitude, due to the close proximity of the ions to the material.

The first device type is used for the optical measurements and this design is characterized by a large grating of gold electrodes on top of a thin layer of Al, which serves as an optical reflector. The Al layer is covered with a 90 nm thick layer of Al_2O_3 and is thus electrically isolated from the gold–electrode

system. In these measurements, we used an ion-containing gel that is, polyethylene glycol (PEG) with a Li$^+$ salt; a Pt/Ag wire was inserted to act as counter and reference electrode, respectively. This gel has the additional advantage that it forms a partial blocking layer for atmospheric oxygen and water. The gate potential was set by applying a potential to the counter electrode with respect to the reference electrode using a potentiostat.

The second device is dedicated to differential capacitance and conductivity measurements. Here, the superlattice is contacted by interdigitated source and drain electrodes, spaced 10 to 100 μm apart, with a total device length between 5 and 1000 mm. The device was topped with anhydrous acetonitrile with 0.1 M lithium perchlorate as salt in which a counter and reference electrode (Pt and Ag wires, respectively) were inserted. For this measurement the PbSe surface was passivated by a PbCl$_2$ treatment. Here again, the gate voltage is set on the counter electrode with respect to the reference electrode using a potentiostat. We measured the potential of the sample vs the Ag reference electrode. An increasingly negative potential on the axis of the figures means that we increase the Fermi-level in our PbSe active layer and, eventually, electron injection sets on.

The final type of chip design consists of several micrometer-sized Hall-bar structures, enabling four-probe conductance measurements. For the four-probe measurements the ionic-liquid DEME-TFSI was used and capped by a thin glass slid to protect the sample from water and oxygen. The potential was set on a Au gate pad evaporated on the chip with reference to the ground.

These different setups and different electrolytes used cause differences in the response of the Fermi-level in the sample to a voltage on the gate. First, the alignment with the vacuum level is different in all setups, and this causes an offset in the gate-axis. Second, there is a difference in the coupling of the voltage on the gate to the shift in Fermi-level.

Determination of the Carrier Density from the Optical Bleach. To quantify electron injection into the PbSe superlattice, its optical absorption was measured during gating. The conduction band occupation of the PbSe superstructures can be monitored by measuring the quenching of the interband absorption. Figure 2a shows the absorption difference at different values of the applied potential for two cyclic potential scans. The second CV cycle almost reproduces the absorption features of the first cycle. This demonstrates that the electrons can be reversibly injected into and extracted from the superlattice. As it is shown in Figure 2b, at potentials more negative than $V_G = -1.22$ V absorption quenching sets in, first at low photon energy between 0.55 and 0.8 eV related to the $1S_h1S_e$ transition. With more negative potentials ($V_G = -1.46$ to -1.69 V), the quenching obtains more weight and also extends to higher photon energies. At even more negative potentials, absorption quenching saturates in the energy region 0.55−0.8 eV. This is illustrated by the inset in Figure 2b where the fractional absorptance versus applied potential is plotted for both the S−S and P−P transitions. We observe that $\frac{\Delta A}{A}$ becomes equal to 1 at a potential of $V_G = -1.53$ for the S−S transition. Concomitantly, the absorption quenching in the range 0.8 to 1.2 eV becomes gradually more important with more negative gate potentials. This feature can be related to $1P_h1P_e$ transition.

The gradual increase and saturation of the bleach feature can be understood by a progressive filling of the 8-fold degenerate
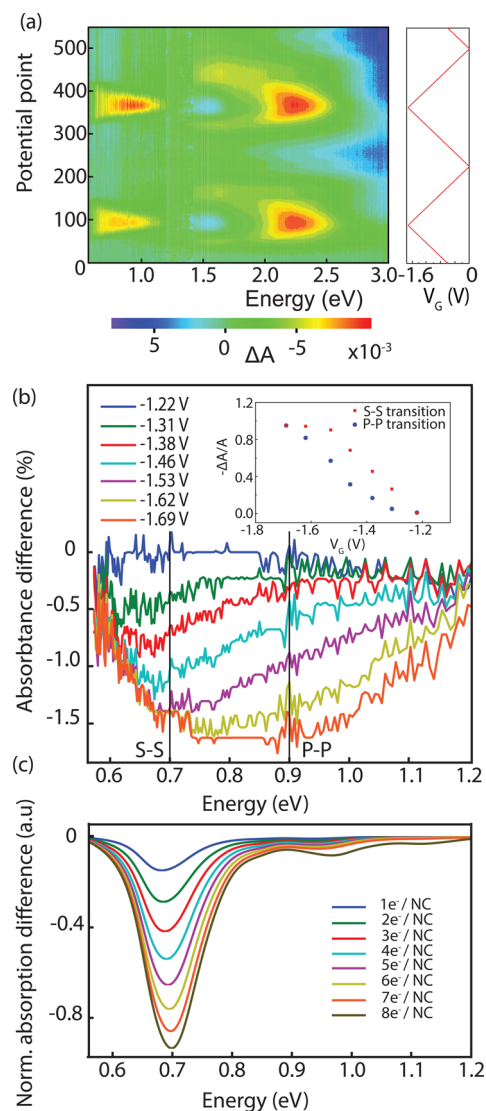

Figure 2. (a) Changes in the absorptance on sweeping the gate twice between $V_G = 0$ and -1.6 V. (b) The absorptance quenching measured at more and more negative potentials; electron injection starts at $V_G = -1.22$ V (dark blue curve) that can be seen as a reference. With more negative potentials, the quenching initially becomes more dominant at low-photon energy and extends to the high-energy range for the most negative potentials applied. Inset: relative differential absorption for the S−S and P−P transitions at energies of 0.7 and 0.9 eV, respectively. (c) Tight-binding calculation of the absorption quenching on the basis of the band structure presented in Figure 1b.

S-type conduction band and partial occupation of the P-band, due to thermal activation at 300 K. The band structure for a 2D PbSe square superlattice has been calculated by Kalesaki et al.;[28] we remark here that the degeneration is lifted by coupling, resulting in four 2-fold degenerate S-bands that are weakly separated. The resulting quenching spectrum upon electron occupation of the S-bands with one to eight electrons is presented in Figure 2c. The main features of the absorption quenching, that is, the gradual shift of the quenching peak to higher energies, the saturation at the low-energy side, and the upcoming quenching of the P−P transition at more negative potentials are all well captured by the calculations.
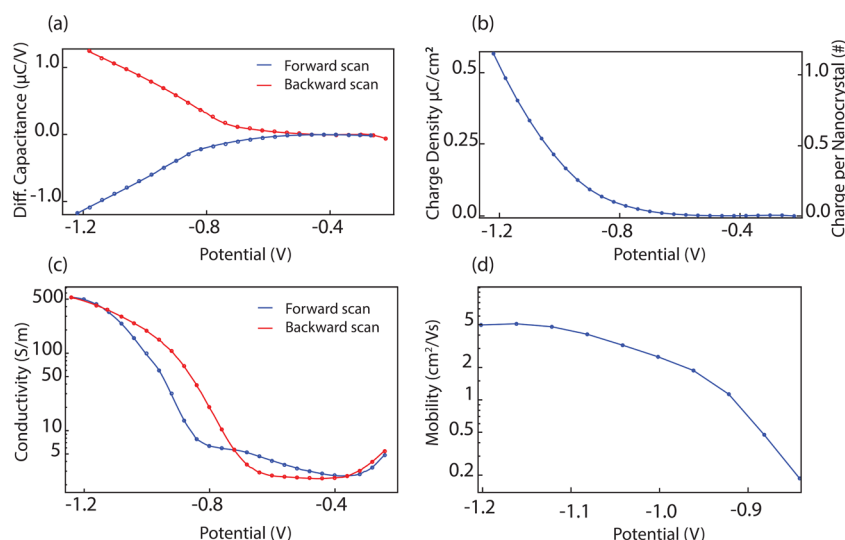
Figure 3. (a) Differential capacitance of a PbSe superstructure measured in forward (from −0.2 to −1.2 V) and backward scan. (b) Charge density and charge per nanocrystal of the PbSe superstructure in the forward scan. (c) The conductivity obtained from the source-drain current and the geometry of the gap (on a logarithmic scale). (d) Electron mobility of the superstructure at the potentials where the Fermi level is above the band gap (logarithmic scale).

It should be noticed that the energy width of the absorption bleach (0.55−1.2 eV) is about twice that of the voltage region over which quenching occurs ($V_G = −1.22$ to $−1.62$ V). This reflects that the band occupation involves the conduction band only but results in quenching of optical transitions from the valence to conduction bands, both bands having a nearly symmetric energy-wave vector dispersion.

At a photon energy of 0.7−0.8 eV, the quenching saturates at a potential of $V_G = −1.53$ V (Figure 2b) to a value of 1.4% in close agreement with 1.5% absorptance of the superstructure (Figure 1b). At more negative potentials, the quenching extends to photon energies between 0.9 and 1.2 eV, that is, quenching of the P−P transition indicating the onset of occupation of the P-bands.

In Figure 2a, two other features can also be distinguished. First, we observe a high energy bleach in the range between 2.0 to 2.5 eV. In the SI (Figure S5), we present TB calculations, which suggest that this feature can be related to the transition of the second L valley in the valence band of bulk PbSe to the lowest state in the conduction band. Second, in the range 1.45 to 1.65 eV, we observe a positive signal that can possibly be attributed to induced absorption. However, interpretation of these features may be affected by the relative strong background.

Differential Capacitance and Conductivity Measurement. To qualify the electron injection into the superlattice, we measured the differential capacitance as a function of the gate voltage. The PbSe superlattices were either as prepared or passivated with $PbCl_2$. We observed that in general the injection and extraction of electrons occurred in a more reversible way with the passivated superlattices. A typical example is presented in Figure 3.

Figure 3a shows the differential capacitance acquired between $V_G = −0.2$ and $−1.2$ V. Electron injection sets in at $V_G = −0.7$ V, meaning that the channels Fermi level crossed the conduction band. In the backward scan, the Fermi level went below the conduction band approximately at the same potential. However, asymmetry in the differential capacitance curve indicates a loss of electrons by an electrochemical process

related to the impurity of the electrolyte solution or the trap states of the superstructure itself. The charge density and the number of charge per NC in the forward scan at every gate potential is displayed in Figure 3b. At the most negative potential in this experiment ($V_G = −1.2$ V), one electron on average was injected to each NC. In this experiment, the uncertainty of the electron density is relatively large because the value of the charge density is calculated based on an estimation of the number of NC sites on the gated part of the PbSe superlattice (more details in the Supporting Information).

In order to investigate the conductivity of the superstructure, the source-drain current upon applying a small bias of 25 mV in a two-probe configuration was recorded. The resulting current−voltage curves are Ohmic when the Fermi level is in the conduction band and their slopes give the conductance (see Figure S6). From the conductance and the geometry of the gap, the conductivity of the PbSe superlattice can be obtained as a function of the gate potential (see conductivity and mobility calculation in Supporting Information). As illustrated by Figure 3c the conductivity sets in at $V_G = −0.7$ V and increases to 500 S/m at $V_G = −1.2$ V. The small value observed in the band gap region is related to the faradaic current.

The electron mobility calculated from the charge density and conductivity rises to a maximum of about 5 cm^2/(V s) at a potential of $V_G = −1.1$ V and stays constant at more negative potential (see Figure 3d). We measured several different samples and found similar values of electron mobility. It should be mentioned that on more "sensitive" devices (i.e., longer finger length) the measured mobility can be smaller due to a significant contribution of the contact resistance to the total conductance. The influence of such contact resistance was also observed in previous works.[23,34]

Four-Probe Measurements. In order to study the 2D square superlattice in small and more homogeneous parts, Hall-bar shaped devices were fabricated (schematic shown in the inset of Figure 4b). This device geometry enables to study the two-probe and four-probe conductance. The two-terminal measurements are performed over the inner contacts (2 μm by 16 μm). Four-terminal measurements were performed by
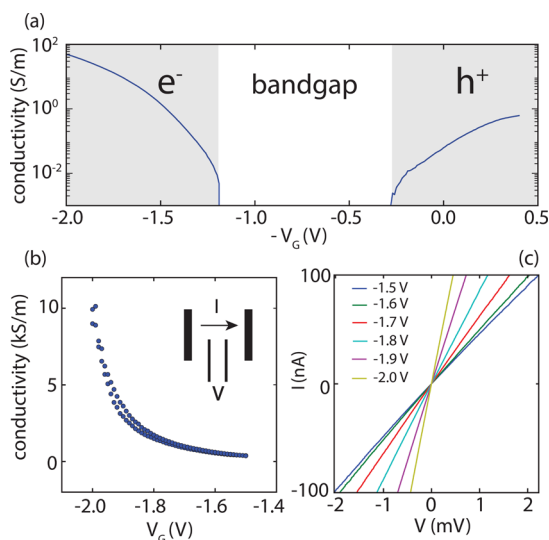
Figure 4. (a) Two-probe conductivity on a log-scale. The insulating region is due to the band gap of the PbSe superlattices. (b) The conductivity measured as a function of the gate voltage under conditions of electron injection. The conductivity was measured by setting a constant current of 10 nA between the two outer contacts while measuring the resulting voltage between the two inner contacts. The gated PbSe superlattice has dimensions of 2 μm (distance between the probes) by 16 μm (width of the channel). (c) Current between the outer contacts versus the voltage measured on the inner contacts for different gate voltages, showing that the current–voltage relationship is linear at all electron densities. In this measurement, the gate voltage is applied on the liquid gate pad.

sending a current across the two outer contacts while measuring the potential difference between the two inner contacts. The results for the resistance in the electron conduction channel are summarized in Table S1. We found that the contact resistance varies from device to device, and dominates in all devices with values ranging between 300 kΩ to 30 MΩ.

To estimate the gate-efficiency in the Hall bar field-effect devices, we measured the ambipolar operation of the field-effect transistors. In Figure 4a, the source drain two-probe conductivity is shown on a log-scale; the rise of the conductance observed at voltages below $V_G = -1.2$ V shows that electrons are injected in the conduction band. In addition, a linear source-drain conductance is also observed at voltages positive of $V_G = -0.3$ V indicating the injection of holes in the highest valence band. The ambipolar operation of the electrolyte gated transistor enables us to relate the insulating gap between $V_G = -1.2$ and -0.3 V to the band gap of the PbSe superlattice. However, to obtain the single-particle gap it has to be corrected for the gate efficiency. Assuming a linear response of the carrier density on to the gate voltage, that is, efficient screening and small charging energies, the gate efficiency is found to be about 0.8 eV/V.

The presence of a sizable contact resistance means that the mobility is underestimated in two-terminal measurements of small devices. We therefore performed four-terminal measurements to obtain a more accurate estimation of the intrinsic mobility. Figure 4b shows the gate response of the four-probe conductance in the electron conduction channel. We observe a dramatic increase in conductance when ramping up the gate. Figure 4c shows the linear IV characteristics, from which we calculate the conductance and the mobility given the electron

density estimated from the optical bleach experiments. Because the complete absorption bleach of the first optical transition occurs at full occupation of the lowest eight bands, the electron density is thus estimated as 8 electrons/NC. We estimate the number of NCs from TEM images to be 2.9×10^{12} NCs/cm^2, giving 2.3×10^{13} electrons/cm^2. The four-probe mobility of the 13 devices spread over 5 different substrates that were investigated are presented in Table S1; the values vary between 1 and 18 cm^2/(V s).

Discussion. Electron and hole transport in self-assembled nanocrystal solids has been studied in the last two decades both for the intrinsic transport physics as for the possible use of these systems in optoelectronic devices.[1−12] Roughly spoken, we can distinguish three classes of quantum dot solids: The first class consists of NC solids as obtained from a NC dispersion by solvent evaporation or addition of a bad solvent. In these NC solids, the surfaces of the nanocrystals remain capped with the organic ligands. The electron tunnelling barriers between adjacent NCs are thus 1−2 times the length of the capping molecules, amounting to 1−3 nm. Such barriers result in a weak coupling between the NCs. Transport characterization in such systems show carrier mobilities below 0.1 cm^2/(V s), limited mainly by carrier tunneling between the localized nanocrystal energy levels. In the second class of solids, the width and the height of the tunneling barriers is reduced by replacing the organic ligands by a variety of short (in)organic ligands. In these systems, the carrier mobility is drastically enhanced to above 1 cm^2/(V s). In some cases, values of 20 cm^2/(V s) are reached;[35,36] the increase of the mobility with decreasing temperature points to band-type transport.[11,14,37,38] In other words, the quantum coupling is sufficiently strong to result in (mini)bands.[28,30] Transport of the carriers in minibands is then limited by scattering to phonons.

The system that we report on here belongs to the third class of solids. Nanocrystals of the Pb-chalcogenide compounds have a rock-salt crystal structure and a truncated cubic or truncated octahedral shape. The oleic acid capping on the {100} facets is weakly bound and desorption of the capping can result in two-dimensional and three-dimensional solids in which the nanocrystals are epitaxially connected with the occurrence of atomically coherent domains of variable size.[13−15] Atomistic theory shows that minibands arise that depend on the geometry of the superlattice. In quasi 2D structures with a square arrangement of the PbSe NCs, Whitham et al.[29] observed mobilities in the order of 0.5 cm^2/(V s).

Here, we report the first study of electron transport in a 2D system with square geometry, in which band occupation is ensured by the high electron densities between 1 and 8 electrons/NC site. Such high electron densities in 2D systems are typical for 2D systems that are electrolyte gated.[16,17] The electron mobility observed here between 5 and 18 cm^2/(V s) is comparable to the those observed in the second class of NC solids (see above). The temperature-dependence of carrier transport will reveal if band like transport is obtained in these systems. We should remark here that the transistor mobilities that we report are roughly an order of magnitude smaller than those obtained from terahertz spectroscopy.[39] With the latter method, transport is probed over a length of only a few nanocrystals. We should hence conclude that the mobilities for long-range transport reported here are most likely still limited by structural defects and the size of the atomic coherent domains.

■ ASSOCIATED CONTENT

⑤ Supporting Information

The Supporting Information is available free of charge on the ACS Publications website at DOI: 10.1021/acs.nano-lett.7b01348.

> Oriented attachment. Electrode designs of all optoelctrochemical gating measurements. Tight-binding calculations. High energy bleach. Conductivity and mobility calculation. Conductivity and mobility calculation in four-probe measurements (PDF)

■ AUTHOR INFORMATION

Corresponding Author

*E-mail: d.vanmaekelbergh@uu.nl.

ORCID ⊙

V. A. E. C. Janssen: 0000-0002-3172-5448

C. Delerue: 0000-0002-0427-3001

L. D. A. Siebbeles: 0000-0002-4812-7495

D. Vanmaekelbergh: 0000-0002-3535-8366

Author Contributions

[⊥]M.A.J. and V.AE.C.J.contributed equally to this work.

Notes

The authors declare no competing financial interest.

■ ACKNOWLEDGMENTS

■ REFERENCES

(1) Drndić, M.; Jarosz, M.; Morgan, N.; Kastner, M.; Bawendi, M. *J. Appl. Phys.* **2002**, *92*, 7498−7503.

(2) Woo, W.-K.; Shimizu, K. T.; Jarosz, M. V.; Neuhauser, R. G.; Leatherdale, C. A.; Rubner, M. A.; Bawendi, M. G. *Adv. Mater.* **2002**, *14*, 1068−1071.

(3) Yu, D.; Wang, C.; Wehrenberg, B. L.; Guyot-Sionnest, P. *Phys. Rev. Lett.* **2004**, *92*, 216802.

(4) Talapin, D. V.; Murray, C. B. *Science* **2005**, *310*, 86−89.

(5) Vanmaekelbergh, D.; Liljeroth, P. *Chem. Soc. Rev.* **2005**, *34*, 299−312.

(6) Law, M.; Luther, J. M.; Song, Q.; Hughes, B. K.; Perkins, C. L.; Nozik, A. J. *J. Am. Chem. Soc.* **2008**, *130*, 5974−5985.

(7) Khon, E.; Lambright, S.; Khon, D.; Smith, B.; O'Connor, T.; Moroz, P.; Imboden, M.; Diederich, G.; Perez-Bolivar, C.; Anzenbacher, P. *Adv. Funct. Mater.* **2012**, *22*, 3714−3722.

(8) Oh, S. J.; Berry, N. E.; Choi, J.-H.; Gaulding, E. A.; Paik, T.; Hong, S.-H.; Murray, C. B.; Kagan, C. R. *ACS Nano* **2013**, *7*, 2413−2421.

(9) Crooker, S.; Hollingsworth, J.; Tretiak, S.; Klimov, V. *Phys. Rev. Lett.* **2002**, *89*, 186802.

(10) Roest, A. L.; Houtepen, A. J.; Kelly, J. J.; Vanmaekelbergh, D. *Faraday Discuss.* **2004**, *125*, 55−62.

(11) Houtepen, A. J.; Vanmaekelbergh, D. *J. Phys. Chem. B* **2005**, *109*, 19634−19642.

(12) Chiu, S.-C.; Jhang, J.-S.; Chen, J.-F.; Fang, J.; Jian, W.-B. *Phys. Chem. Chem. Phys.* **2013**, *15*, 16127−16131.

(13) Liu, W.; Lee, J.-S.; Talapin, D. V. *J. Am. Chem. Soc.* **2013**, *135*, 1349−1357.

(14) Jang, J.; Liu, W.; Son, J. S.; Talapin, D. V. *Nano Lett.* **2014**, *14*, 653−662.

(15) Nag, A.; Zhang, H.; Janke, E.; Talapin, D. V. *Z. Phys. Chem.* **2015**, *229*, 85−107.

(16) Luther, J. M.; Pietryga, J. M. *ACS Nano* **2013**, *7*, 1845−1849.

(17) Gao, Y.; Aerts, M.; Sandeep, C. S. S.; Talgorn, E.; Savenije, T. J.; Kinge, S.; Siebbeles, L. D. A.; Houtepen, A. J. *ACS Nano* **2012**, *6*, 9606−9614.

(18) Sandeep, C. S. S.; Azpiroz, J. M.; Evers, W. H.; Boehme, S. C.; Moreels, I.; Kinge, S.; Siebbeles, L. D. A.; Infante, I.; Houtepen, A. J. *ACS Nano* **2014**, *8*, 11499−11511.

(19) Koh, W.-k.; Saudari, S. R.; Fafarman, A. T.; Kagan, C. R.; Murray, C. B. *Nano Lett.* **2011**, *11*, 4764−4767.

(20) Dong, A.; Jiao, Y.; Milliron, D. J. *ACS Nano* **2013**, *7*, 10978−10984.

(21) Kang, M. S.; Lee, J.; Norris, D. J.; Frisbie, C. D. *Nano Lett.* **2009**, *9*, 3848−3852.

(22) Oh, S. J.; Berry, N. E.; Choi, J.-H.; Gaulding, E. A.; Lin, H.; Paik, T.; Diroll, B. T.; Muramoto, S.; Murray, C. B.; Kagan, C. R. *Nano Lett.* **2014**, *14*, 1559−1566.

(23) Oh, S. J.; Wang, Z.; Berry, N. E.; Choi, J.-H.; Zhao, T.; Gaulding, E. A.; Paik, T.; Lai, Y.; Murray, C. B.; Kagan, C. R. *Nano Lett.* **2014**, *14*, 6210−6216.

(24) Kagan, C.; Murray, C. *Nat. Nanotechnol.* **2015**, *10*, 1013−1026.

(25) Evers, W. H.; Goris, B.; Bals, S.; Casavola, M.; de Graaf, J.; Roij, R. v.; Dijkstra, M.; Vanmaekelbergh, D. *Nano Lett.* **2013**, *13*, 2317−2323.

(26) Boneschanscher, M. P.; Evers, W. H.; Geuchies, J. J.; Altantzis, T.; Goris, B.; Rabouw, F. T.; Van Rossum, S.; van der Zant, H. S.; Siebbeles, L. D.; Van Tendeloo, G.; et al. *Science* **2014**, *344*, 1377−1380.

(27) Schliehe, C.; Juarez, B. H.; Pelletier, M.; Jander, S.; Greshnykh, D.; Nagel, M.; Meyer, A.; Foerster, S.; Kornowski, A.; Klinke, C. *Science* **2010**, *329*, 550−553.

(28) Kalesaki, E.; Evers, W.; Allan, G.; Vanmaekelbergh, D.; Delerue, C. *Phys. Rev. B: Condens. Matter Mater. Phys.* **2013**, *88*, 115431.

(29) Whitham, K.; Yang, J.; Savitzky, B. H.; Kourkoutis, L. F.; Wise, F.; Hanrath, T. *Nat. Mater.* **2016**, *15*, 557−563.

(30) Kalesaki, E.; Delerue, C.; Morais Smith, C.; Beugeling, W.; Allan, G.; Vanmaekelbergh, D. *Phys. Rev. X* **2014**, *4*, 011010.

(31) Geuchies, J. J.; Van Overbeek, C.; Evers, W. H.; Goris, B.; De Backer, A.; Gantapara, A. P.; Rabouw, F. T.; Hilhorst, J.; Peters, J. L.; Konovalov, O.; et al. *Nat. Mater.* **2016**, *15*, 1248−1254.

(32) Wolcott, A.; Doyeux, V.; Nelson, C. A.; Gearba, R.; Lei, K. W.; Yager, K. G.; Dolocan, A. D.; Williams, K.; Nguyen, D.; Zhu, X.-Y. *J. Phys. Chem. Lett.* **2011**, *2*, 795−800.

(33) Fang, H.; Bechtel, H. A.; Plis, E.; Martin, M. C.; Krishna, S.; Yablonovitch, E.; Javey, A. *Proc. Natl. Acad. Sci. U. S. A.* **2013**, *110*, 11688−11691.

(34) Luther, J. M.; Law, M.; Beard, M. C.; Song, Q.; Reese, M. O.; Ellingson, R. J.; Nozik, A. J. *Nano Lett.* **2008**, *8*, 3488−3492.

(35) Lee, J.; Kovalenko, M.; Huang, J.; Chung, D.; Talapin, D. *Nat. Nanotechnol.* **2011**, *6*, 348−352.

(36) Chung, D. S.; Lee, J.-S.; Huang, J.; Nag, A.; Ithurria, S.; Talapin, D. V. *Nano Lett.* **2012**, *12*, 1813−1820.

(37) Choi, J.-H.; Fafarman, A. T.; Oh, S. J.; Ko, D.-K.; Kim, D. K.; Diroll, B. T.; Muramoto, S.; Gillen, J. G.; Murray, C. B.; Kagan, C. R. *Nano Lett.* **2012**, *12*, 2631−2638.

(38) Talgorn, E.; Gao, Y.; Aerts, M.; Kunneman, L. T.; Schins, J. M.; Savenije, T.; Van Huis, M. A.; Van der Zant, H. S.; Houtepen, A. J.; Siebbeles, L. D. *Nat. Nanotechnol.* **2011**, *6*, 733−739.

(39) Evers, W. H.; Schins, J. M.; Aerts, K. A. M.; Capiod, P.; Berthe, M.; Grandidier, B.; Delerue, C.; van der Zant, H. S. J.; van Overbeek, C.; Peters, J. L.; Vanmaekelbergh, D.; Siebbeles, L. D. A. *Nat. Commun.* **2015**, *6*, 1−8.